

## A hybrid integrated high-precision tunable semiconductor laser

Yiran Zhu, Botao Fu, Zhiwei Fang, Qiyue Hu, Jianping Yu, Yunpeng Song, Yu Ma, Min Wang, Kunpeng Jia, Zhenda Xie\* and Ya Cheng\*

**Citation:** Zhu YR, Fu BT, Fang ZW, Hu QY, Yu JP, Song YP, Ma Y, Wang M, Jia KP, Xie ZD, Cheng Y. A hybrid integrated high-precision tunable semiconductor laser. *Opto-Electron Adv* **9**, 250274 (2026).

<https://doi.org/10.29026/oea.2026.250274>

Received: 13 October 2025; Accepted: 10 December 2025; Published online: 5 February 2026

### Related articles

High fiber-to-fiber net gain in erbium-doped thin film lithium niobate waveguide amplifier as an external gain chip

Jinli Han, Mengqi Li, Rongbo Wu et al

*Opto-Electronic Science* 2025, **4**(9): 250004 doi: [10.29026/oes.2025.250004](https://doi.org/10.29026/oes.2025.250004)

Thin-film lithium niobate-based detector: recent advances and perspectives

Xiaoli Sun, Yuechen Jia, Feng Chen

*Opto-Electronic Science* 2025, **4**(12): 250028 doi: [10.29026/oes.2025.250028](https://doi.org/10.29026/oes.2025.250028)

Strong-confinement low-index-rib-loaded waveguide structure for etchless thin-film integrated photonics

Yifan Qi, Gongcheng Yue, Ting Hao et al

*Opto-Electronic Advances* 2025, **8**(9): 250056 doi: [10.29026/oea.2025.250056](https://doi.org/10.29026/oea.2025.250056)

Soliton microcomb generation by cavity polygon modes

Botao Fu, Renhong Gao, Ni Yao et al

*Opto-Electronic Advances* 2024, **7**(8): 240061 doi: [10.29026/oea.2024.240061](https://doi.org/10.29026/oea.2024.240061)

More related articles in Opto-Electronic Journals Group website



# A hybrid integrated high-precision tunable semiconductor laser

Yiran Zhu<sup>1,2</sup>, Botao Fu<sup>2</sup>, Zhiwei Fang<sup>2</sup>, Qiyue Hu<sup>1,2</sup>, Jianping Yu<sup>2</sup>, Yunpeng Song<sup>2</sup>, Yu Ma<sup>3</sup>, Min Wang<sup>2</sup>, Kunpeng Jia<sup>4</sup>, Zhenda Xie<sup>4\*</sup> and Ya Cheng<sup>2\*</sup>

**Abstract:** Thin-film lithium niobate has become a promising platform for integrated photonics due to its outstanding electro-optic and nonlinear properties. However, the development of on-chip tunable lasers, which is essential for a plethora of applications ranging from optical communications and sensing to metrology and quantum technology, remains limited. Current solutions fall short in either wavelength tuning range or precision, and frequently relies on complex control strategy. Here, we demonstrate an integrated electro-optically tunable narrow-linewidth III-V laser, achieving a tuning range of  $\sim 51.8$  nm, an intrinsic linewidth of  $\sim 1.21$  MHz, and high tuning precision of  $\sim 0.03$  nm. Specifically, our external cavity uniquely combines highly reflective Sagnac mirrors and a series of unbalanced interferometers which together offer a spectral response in favor of single-longitudinal-mode narrow-linewidth lasing operation, evidenced by not only experimental demonstration but also insightful theoretical analysis.

**Keywords:** hybrid integrated laser; high-precision tuning semiconductor laser; thin-film lithium niobate

DOI: [10.29026/oea.2026.250274](https://doi.org/10.29026/oea.2026.250274) | CSTR: [32247.14.oea.2026.250274](https://cstr.cn/32247.14.oea.2026.250274)

**Citation:** Zhu YR, Fu BT, Fang ZW et al. A hybrid integrated high-precision tunable semiconductor laser. *Opto-Electron Adv* 9, 250274 (2026).

## 1 Introduction

Miniaturized wavelength tunable lasers of narrow linewidth, wide tuning range and high tuning speed and efficiency are highly in demand for a plethora of applications ranging from optical communications and sensing to metrology and quantum technology<sup>1-7</sup>. Thanks to the rapid development of photonic integration technique, external cavities lasers composed of photonic integrated circuits (PICs) and semiconductor optical amplifiers (SOA) provide a promising solution to realizing compact and low power consumption narrow-linewidth lasers. So far, most on-chip tunable laser solutions that hybrid integrate SOA chips with PICs typically utilize one or two tunable, micro-ring resonators<sup>8-23</sup>. However, limited by the free spectral range (FSR) and the high out-of-band rejection ratio of micro-ring resonators, it is generally difficult to attain laser tuning precision at the 0.1 nm scale. Achieving high-precision tuning across wide spectra thus remains challenging.

Recently, low-loss waveguides, micro cavities and electro-

optic modulators based on thin-film lithium niobate (TFLN)<sup>24-28</sup> have been intensively investigated because TFLN has prominent ultra-wide optical bandwidth and ultra-high electro-optic efficiency<sup>29-41</sup>. In this work, we propose a unique tunable Sagnac loop reflector (TSLR) based on TFLN composed of an unbalanced Michelson interferometer (MI), unbalanced Mach-Zehnder interferometers (MZIs) and Sagnac loop mirrors<sup>42-44</sup>. By directly butt-coupling TSLR with a C-band high-reflectivity semiconductor optical amplifier (RSOA), we construct a tunable Fabry-Pérot cavity laser. The laser realizes a single-mode output with a maximum on-chip power of 102.7  $\mu$ W and an intrinsic linewidth of  $\sim 1.21$  MHz. The laser incorporates both electro-optic tuning and thermo-optic tuning. This combination achieves a wide tuning range of  $\sim 51.8$  nm, with the highest tuning precision of 0.03 nm and continuous tuning range of  $\sim 3.5$  pm. This design successfully realizes a stable wide-range, high-precision, single-mode on-chip tunable laser. Furthermore, we reformulate a theory of

Received: 13 October 2025

Accepted: 10 December 2025

Published online: 5 February 2026

<sup>1</sup>State Key Laboratory of Precision Spectroscopy, East China Normal University, Shanghai 200241, China; <sup>2</sup>The Extreme Optoelectromechanics Laboratory (XXL), School of Physics, East China Normal University, Shanghai 200241, China; <sup>3</sup>State Key Laboratory of High Field Laser Physics and CAS Center for Excellence in Ultra-intense Laser Science, Shanghai Institute of Optics and Fine Mechanics (SIOM), Chinese Academy of Sciences (CAS), Shanghai 201800, China; <sup>4</sup>National Laboratory of Solid State Microstructures, School of Electronic Science and Engineering, College of Engineering and Applied Sciences, Nanjing University, Nanjing 210023, China.

\*Correspondence: ZD Xie, E-mail: [xiezhenda@nju.edu.cn](mailto:xiezhenda@nju.edu.cn); Y Cheng, E-mail: [ya.cheng@siom.ac.cn](mailto:ya.cheng@siom.ac.cn)

semiconductor lasers, which shed new light on hybrid integrated high-precision tunable lasers.

## 2 Design and theoretical analysis

### 2.1 The design of hybrid integrated laser

As shown in Fig. 1(a), RSOA (AE5T315BY20P, Anritsu), which provides the electrically pumped optical gain, is a C-band single-angled facet gain chip incorporated with curving ridge waveguide and an anti-reflection coating to suppress the reflection. On the other side, a reflection coating with approximately 95% reflectivity serves as an end mirror of the F-P cavity. The TSLR is fabricated on an 800 nm thick TFLN substrates (800 nm thickness TFLN, 2 μm thickness SiO<sub>2</sub>, and 525 μm thickness Si, NANOLN) using the photolithography assisted chemo-mechanical etching (PLACE) technique<sup>45–48</sup>. More technical details of PLACE and the fabricated TFLN chip can be found in the Supplementary Information.

Figure 1(b) illustrates the main architecture of our laser, which consists of an RSOA and two TSLRs on TFLN. The Sagnac loop reflector (SLR) are formed by connecting the two output ports of the 2×2 3 dB couplers to create a loop path. Here, we construct the 2×2 3 dB couplers simply with directional couplers (DCs). When the two outputs beams propagate through the loop, they both introduce a phase delay. The two beams interfere upon passing through the

DC again. When two light beams generate the π/2 phase shift and the coupling ratio of DC is 50:50<sup>49</sup>, almost all of the light returns to the input waveguide so that the Sagnac loop reflector can behave as a perfect reflecting mirror. The reflection coating on the left end of RSOA and the Fresnel reflection at the interface of RSOA and TFLN chip form a low Q F-P cavity with an FSR of 0.2852 nm, providing a coarse mode selection capability. On the other side, the two TSLRs are in parallel and combined into a Michelson interferometer using a 3 dB DC. The Michelson interferometer is intentionally designed to be unbalanced with a small length difference of 100 μm between the two arms. The two TSLRs form two cavities with the interface of RSOA and TFLN chip, respectively, featuring slightly different FSRs of 0.0283 nm and 0.0282 nm. Such configuration effectively results in a Vernier effect that enables narrow-band mode selection over a wide spectral range. The lower panel of Fig. 1(b) shows the combined effect on mode selection of these three cavities.

The TSLRs have a broad reflection bandwidth. The reflectivity of the Sagnac loop reflector gradually decreases from nearly 100% at 1550 nm to 95% at 1520 nm and 1580 nm. For further improving the fine-tuning ability of our laser, we add electrically-tunable MZIs and Michelson interferometer into the main architecture of the external cavity. As illustrated in Fig. 1(c), the laser beams returning from the two TSLRs will pass through the two arms of the 100 μm

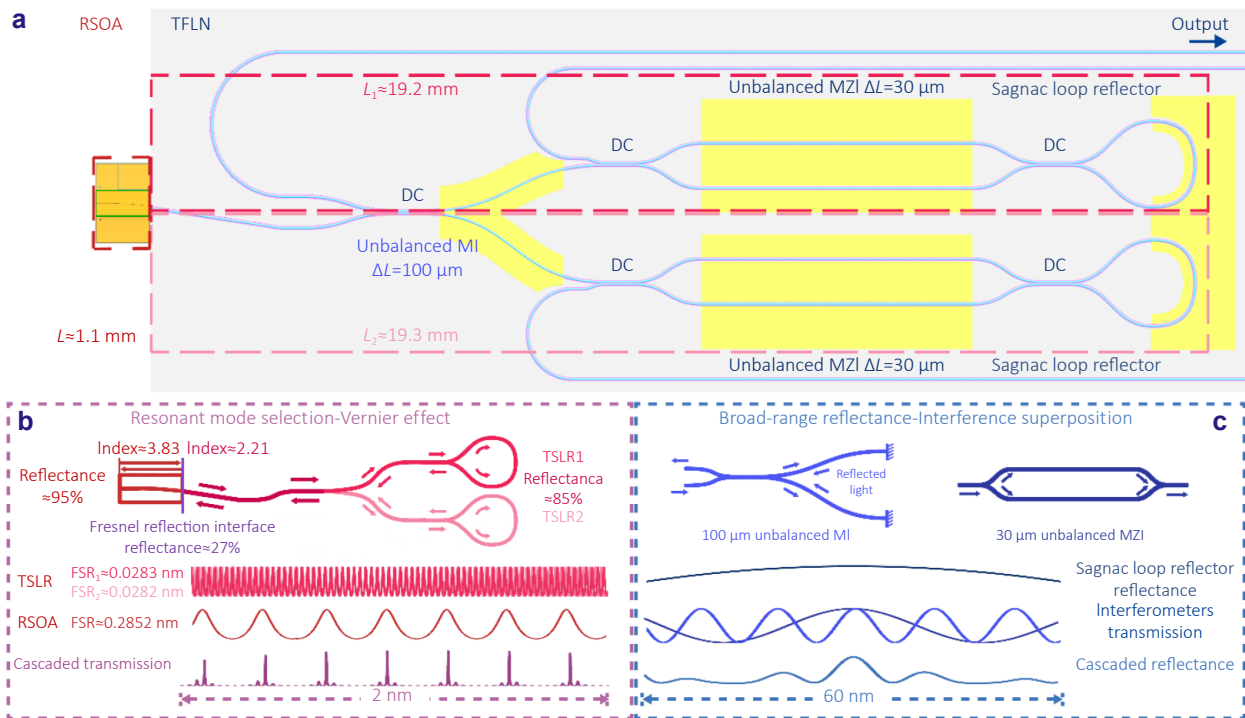


Fig. 1 | Schematic view of the hybrid integrated laser. (a) Schematic view of hybrid integrated III-V laser based on TFLN. (b) Illustration of the Vernier effect by calculating the FSR of the superposed resonances from TSLRs and RSOA. (c) Illustration of the interference superposition by calculating the transmission of interferometers and reflectance of Sagnac loop reflector.

unbalanced Michelson interferometer. In each arm of the Michelson interferometer, the 30 μm unbalanced MZIs is inserted near the TSLR. The 100 μm unbalanced Michelson interferometer and 30 μm unbalanced MZIs will give rise to their characteristic transmission spectrum with modulation periods of 16 nm and 40 nm, respectively. As a result, the interference superposition provides a broad-range reflectivity modulation for the laser mode selection. By applying electro-optic tuning or thermo-optic tuning to three unbalanced interferometers and Sagnac loop reflectors, we realize a tunable on-chip laser with multi-scale wavelength tuning capabilities, as we will demonstrate below in both experiments and theory.

### 2.2 The mode competition calculation of hybrid integrated laser

In the hybrid integrated F-P laser system, one mirror is provided by the reflection coating on one side of the RSOA, while the other one is determined by the TSLR that we designed. The laser cavity size of on-chip lasers is much smaller than that of conventional lasers, resulting in fewer resonant modes. Therefore, we do not require extremely sharp filtering to establish loss differences among all resonant modes in on-chip laser systems.

In a multiple-longitudinal-mode semiconductor laser, the rate equations for carriers under steady-state condition can be approximated as:

$$\sum_m \frac{1}{\left(\frac{N_{th,m}}{N} - 1\right)} = \frac{N_j - N}{N - N_{th,m} + \frac{A_m}{\Gamma a}} \beta, \quad (1)$$

where,  $N_j$ ,  $N$  and  $A_m$  represent the injected carrier density, carrier density and mode loss, respectively. The constant  $a$ ,  $\Gamma$  represent the optical gain factor, the optical confinement factor. The constant  $\beta$  takes the form  $\beta = \frac{\Gamma \lambda_e^4}{4\pi^2 n^3 V \Delta \lambda}$ , representing the spontaneous emission factor, in which  $V$  represents the active region volume.  $N_{th,m}$  represent threshold carrier density, and the fundamental mode ( $m=0$ ) achieves a minimized threshold carrier density among all longitudinal modes.

Under the condition  $N_j \gg N_{th}$ , the solution exists for  $\sum_m \left(\frac{N_{th,m}}{N} - 1\right)^{-1} \gg 0$ . As illustrated in Fig. 2(a), ansatz  $N = N_{th,0} - \varepsilon$ ,  $\varepsilon$  can be expressed as:

$$\varepsilon \cong \frac{A\beta}{\Gamma^2 a} \frac{1}{N_j - N_{th,0}} = \beta_{eff} \frac{1}{N_j - N_{th,0}}. \quad (2)$$

The photon densities of different resonant modes  $S_m$  can be expressed as:

$$S_m \cong \frac{n\beta_{eff} N_{th,0}}{ac\tau} \frac{1}{N_{th,m} - N_{th,0} + \varepsilon} = \frac{n\beta_{eff}}{ac\tau} \frac{1}{\left(\frac{N_{th,m}}{N} - 1\right)}, \quad (3)$$

where,  $\tau$  represents carrier lifetime, the constant  $c$ ,  $n$  represent the speed of light in vacuum and the refractive index of the medium.

So, the photon densities of different resonant modes are determined by  $\left(\frac{N_{th,m}}{N} - 1\right)^{-1}$ . Therefore, when the optical gain exceeds the minimum threshold, fundamental mode effectively suppresses competing modes through gain clamping effect. As illustrated in Fig. 2(b), the lowest threshold results in the highest photon density and the limited photons are redistributed to other modes. So, the single-mode lasing will be triggered, as shown in Fig. 2(c). This constitutes the fundamental mechanism of mode competition. In principle, mode competition and gain narrowing originate from the same physical mechanism<sup>43</sup>. The resolution of mode competition can be quantified by utilizing  $Q$  factors, spectral linewidths  $\delta\omega$  and mode decay rate  $\gamma$  as:

$$\eta = 1 - \frac{|\delta\omega + iy|}{\gamma} \cong \frac{\delta\omega}{\gamma} \propto \frac{1}{Q}. \quad (4)$$

Hybrid integrated F-P resonators typically exhibit high  $Q$ -factor, enabling the realization of mode threshold disparity using filters with gradual spectral transitions, such as unbalanced interferometers. Detailed calculations can be found in the Supplementary information. As shown in Fig. 2(d) and Fig. 2(e), we can calculate the cavity  $Q$ -factor by neglecting external cavity transmission loss and coupling loss. By applying a  $\pi$ -phase shift to the 30 μm MZI and 100 μm unbalanced MI, the wavelength corresponding to the peak  $Q$ -factor can be dynamically tuned 17 nm and 10 nm through phase modulation, respectively. Instead, the limited tuning range of a single unbalanced MZI can be substantially extended through connecting two 30 μm unbalanced MZIs in parallel using non-commensurate 100 μm unbalanced Michelson interferometer. As demonstrated in Fig. 2(f) and Fig. 2(g), the wavelength corresponding to the peak  $Q$ -factor can be tuned over 36 nm through cooperative modulation achieved by simultaneously applying interrelated phase shifts to all unbalanced interferometers. Continuous tuning of the wavelength corresponding to the peak  $Q$ -factor can be achieved by applying fine phase adjustments to the interferometers.

### 3 Results and discussion

In fact, it is known that the transmission loss and coupling loss cannot be totally neglected, resulting in cavity  $Q$ -factor degradation. Despite this, our laser still demonstrates high-resolution  $Q$ -factor discrimination capability. The experimental setup for characterization of the laser performance is

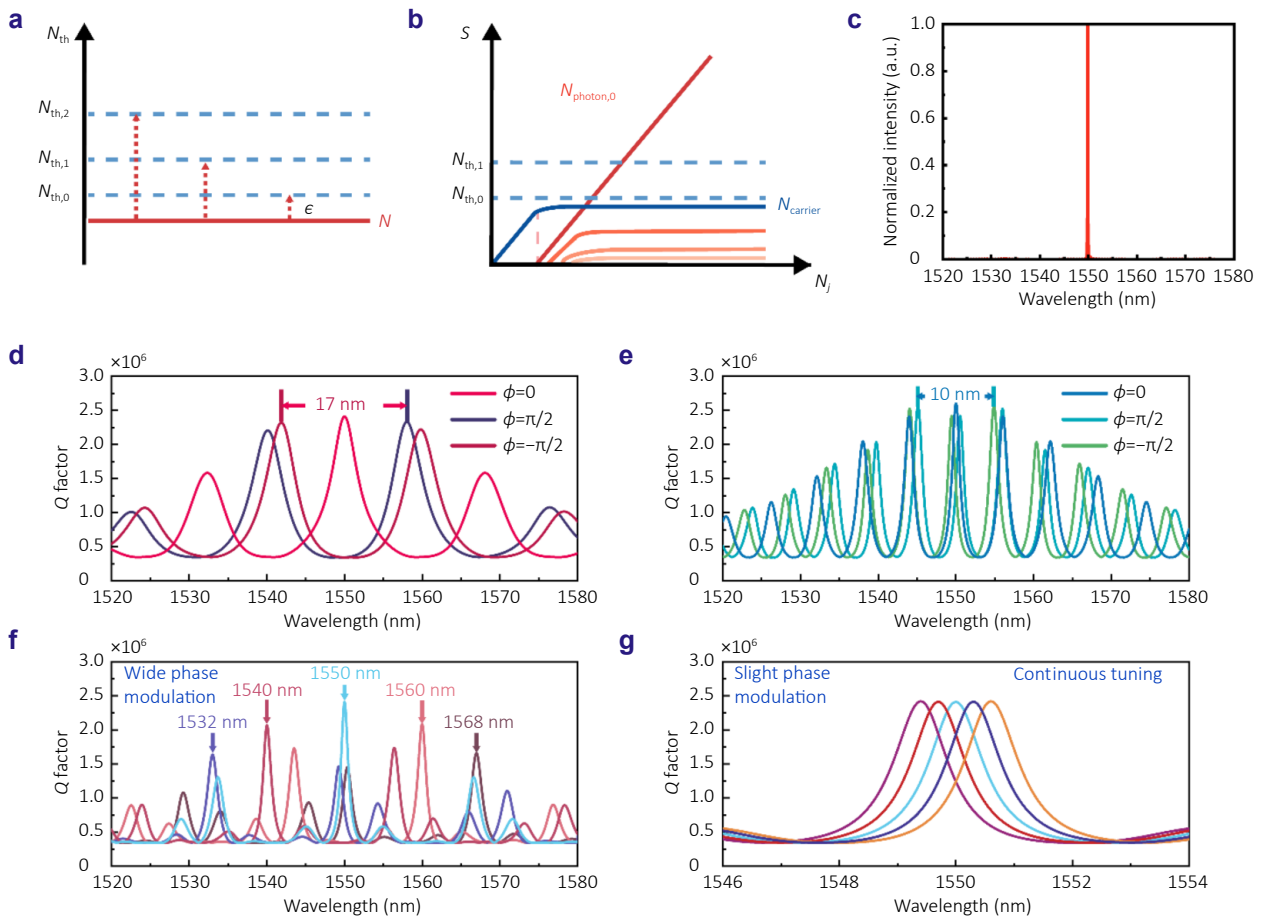


Fig. 2 | Tuning demonstration of the hybrid integrated laser. (a) The threshold carrier density of different longitudinal modes. (b) Mode competition mechanism of semiconductor lasers. (c) The calculated result of triggered single-mode lasing. (d) The theoretical Q-factor modulation of the hybrid integrated F-P resonator integrated with 30  $\mu\text{m}$  unbalanced MZI. (e) The theoretical Q-factor modulation of the hybrid integrated F-P resonator integrated with 100  $\mu\text{m}$  unbalanced MI. (f) Wide cooperative phase modulation of the two 30  $\mu\text{m}$  unbalanced MZIs in parallel using non-commensurate 100  $\mu\text{m}$  unbalanced MI. (g) Slight phase cooperative modulation of all interferometers.

shown in Fig. 3(a). When the 180 mA direct current is applied to RSOA, the integrated laser demonstrates single-mode operation at 1551.59 nm wavelength, as shown in Fig. 3(b), achieving a maximum on-chip power of 102.7  $\mu\text{W}$  with side mode suppression ratio of 39.65 dB. The intrinsic linewidth of the laser is measured as 1.21 MHz using a self-built delayed self-heterodyne interferometer as shown in Fig. 3(c), in which the frequency shift of the acousto-optic modulator (AOM) is 100 MHz. As shown in Fig. 3(d), it is observed that the laser can be stably operated without mode hop for up to 30 minutes as measured using a wavemeter (WS6-200, TOPTICA Photonics). By applying a DC voltage (IPMP250-1 L, INTERLOCK,  $\pm 30$  V) to the MZIs and Michelson interferometer as well as the Sagnac loop reflectors respectively, a tuning range of laser wavelength of 51.8 nm is measured using an optical spectrum analyzer (OSA, AQ6375B, Yokogawa), as shown in Fig. 3(e). Slight variations to the applied voltage enable tuning precision of  $\sim 0.16$  nm, as shown in Fig. 3(f), and even higher precision of  $\sim 0.03$

nm, as shown in Fig. 3(g). The tuning precision is ultimately limited by the FSR of TSLR. The electro-optic tuning modes are discrete resonant modes. Because the gain spectrum of the RSOA and the reflectivity of the TSLRs are not symmetrically centered at 1550 nm, the symmetry of unbalanced MZIs tuning is highly susceptible to disruption. As a result, the actual tuning range exceeds the theoretically predicted 36 nm. To achieve continuous tuning of laser wavelength, we conduct thermo-optic tuning on the Sagnac loop reflector.

While electro-optic tuning enables a broad tuning range, achieving continuous tuning requires the use of thermal tuning due to minimum tuning step of the DC voltage. As shown in Fig. 4(a), We connect a thermal probe with a single electrode on the right-handed side of Sagnac loop reflectors as the heater. In this way, the thermal probe can efficiently heat the gold electrode and in turn raise the temperature of the Sagnac loop for wavelength tuning. Thanks to the excellent thermal conductivity of gold, we realize localized thermal tuning of Sagnac loop reflectors. This configuration of

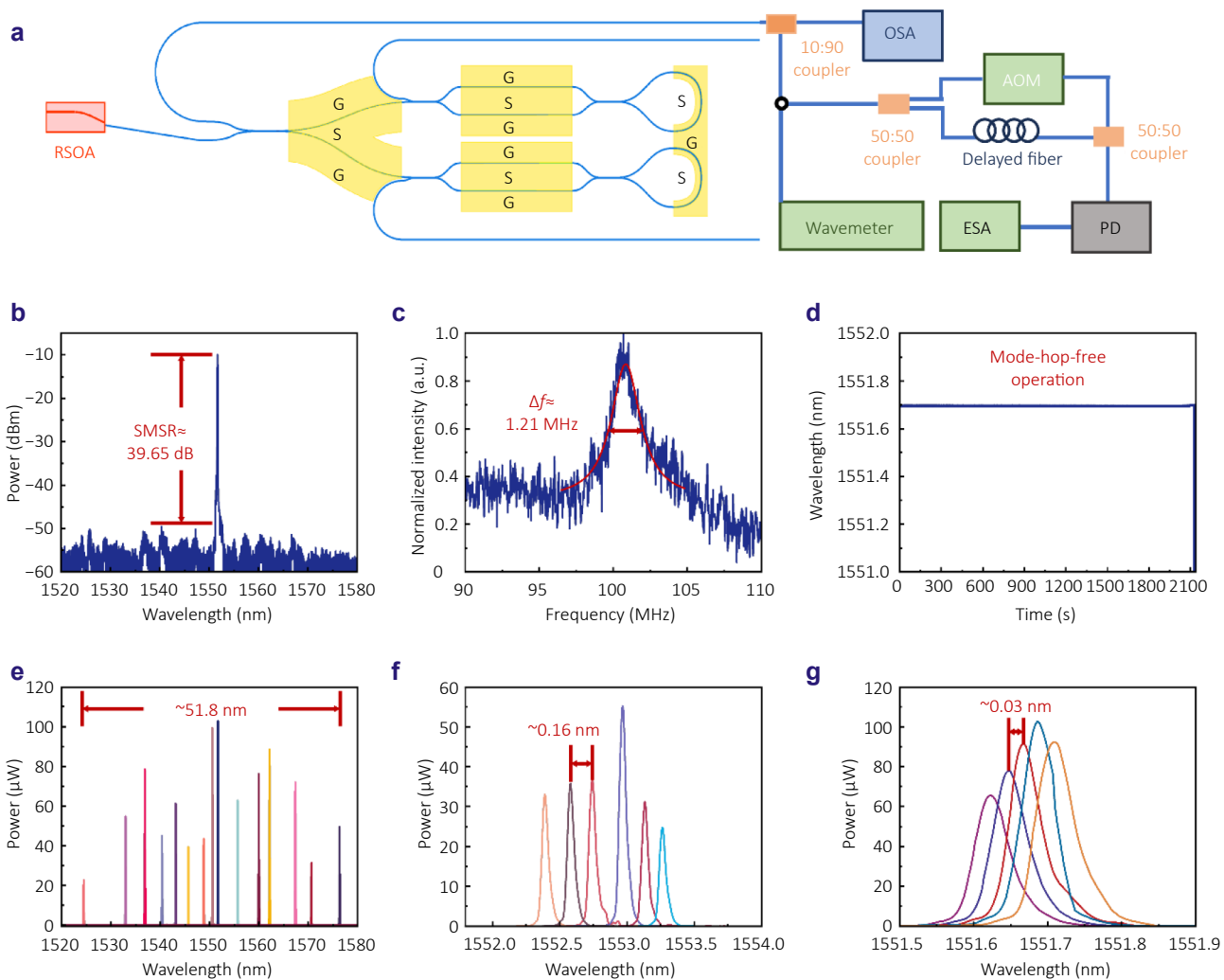


Fig. 3 | Multi-scale wavelength tuning capabilities. (a) Schematic view of laser testing system. (b) Single-mode laser at 1551.59 nm wavelength with a maximum on-chip power of 102.7  $\mu$ W and side mode suppression ratio of 39.65 dB. (c) The linewidth of 1.21 MHz is extracted by a self-built delayed self-heterodyne interferometer. (d) Long term mode-hop- free operation of the laser measured using a wavemeter. (e) The laser exhibits a wide wavelength tunability of 51.8 nm, while the tuning range of DC voltage is  $-30$  V to  $+30$  V. (f) The precise tuning of  $\sim 0.16$  nm scale. (g) The precise tuning of  $\sim 0.03$  nm scale.

two electrodes enables heat to be conducted through the one electrode to the other where it dissipates, effectively confining heat transfer within the Sagnac loop reflectors. Thermal image (VCr580, Infra Tec) shown in Fig. 4(b) confirms that no obvious temperature changes can be observed in MZIs and Michelson interferometer. As illustrated in Fig. 4(c), a continuous tuning range of  $\sim 3.5$  pm can be achieved when the electrode temperature is increased by  $\sim 5$   $^{\circ}$ C through probe heating. Throughout the heating process, we monitor the laser with an OSA to ensure mode-hop-free operation.

### 4 Conclusions

In this work, we demonstrate an integrated TFLN/III-V lasers based on TFLN, achieving a maximum on-chip power of 102.7  $\mu$ W at 1551.69 nm, an intrinsic linewidth of  $\sim 1.21$  MHz, a tuning range of  $\sim 51.8$  nm, a tuning precision of 0.02

nm and continuous tuning range of  $\sim 3.5$  pm. Benefiting from the linear electro-optic response of TFLN and the low-loss TSLR based on TFLN fabricated by the PLACE technique, this unique external cavity can be effectively integrated with RSOA to accomplish a wide-range, high-precision, single-mode on-chip tunable laser. Moreover, our external cavity is exclusively built upon single-mode-waveguide-based photonics structures, ensuring that the laser beam only propagates in the fundamental mode within the resonant cavity without interference from the higher-order modes. This design significantly enhances the operational stability of the lasers while offering wide system-level tolerance, thereby relaxing fabrication requirements. Furthermore, the reformulated theory of semiconductor lasers not only provides design inspiration for hybrid integrated lasers but also offers critical insights into on-chip self-injection locked laser. Since the gain clamping effect does not relies

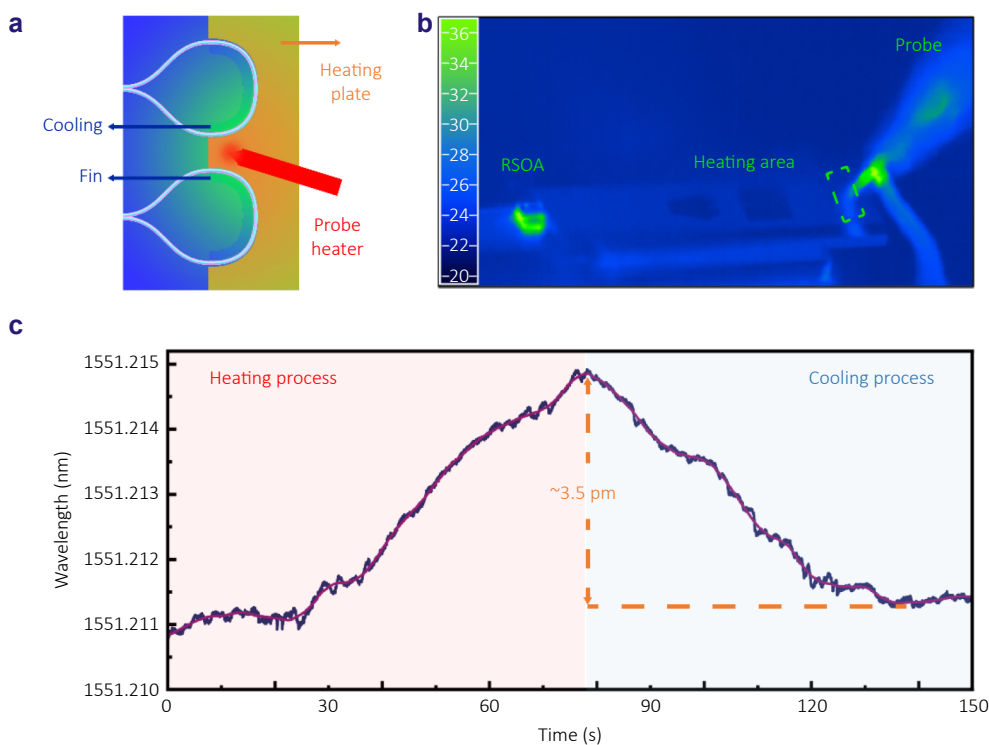


Fig. 4 | Continuous wavelength tuning capability. (a) Schematic view of localized heating. (b) Thermal image of laser continuous tuning testing system. (c) The maximum laser continuous tuning range of  $\sim 3.5$  pm and whole process lasts  $\sim 150$  s.

on the pumping mechanism, i.e., electrical pumping or optical pumping, our theory also provides theoretical guidance for the design of rare-earth-ion-doped monolithic laser. Lastly, the laser output power has significant potential for further improvement. In our future work, we will design and fabricate spot size converters (SSCs) to improve the coupling efficiency between the RSOA and TFLN and between the TFLN and output fiber, with the goal of achieving higher output power and narrower intrinsic linewidth.

## References

- Snigirev V, Riedhauser A, Lihachev G et al. Ultrafast tunable lasers using lithium niobate integrated photonics. *Nature* **615**, 411–417 (2023).
- Guo QS, Gutierrez BK, Sekine R et al. Ultrafast mode-locked laser in nanophotonic lithium niobate. *Science* **382**, 708–713 (2023).
- Ouyang YH, Luan HY, Zhao ZW et al. Singular dielectric nanolaser with atomic-scale field localization. *Nature* **632**, 287–293 (2024).
- Ashtiani F, Geers AJ, Aflatouni F. An on-chip photonic deep neural network for image classification. *Nature* **606**, 501–506 (2022).
- Liang D, Huang X, Kurczveil G et al. Integrated finely tunable microring laser on silicon. *Nat Photonics* **10**, 719–722 (2016).
- Kurosaka Y, Iwahashi S, Liang Y et al. On-chip beam-steering photonic-crystal lasers. *Nat Photonics* **4**, 447–450 (2010).
- Zhang XS, Kwon K, Henriksson J et al. A large-scale microelectromechanical-systems-based silicon photonics LiDAR. *Nature* **603**, 253–258 (2022).
- Franken CAA, Cheng R, Powell K et al. High-power and narrow-linewidth laser on thin-film lithium niobate enabled by photonic wire bonding. *APL Photonics* **10**, 026107 (2025).
- Liu Y, Qiu ZR, Ji XR et al. A fully hybrid integrated erbium-based laser. *Nat Photonics* **18**, 829–835 (2024).
- Tran MA, Huang DN, Bowers JE. Tutorial on narrow linewidth tunable semiconductor lasers using Si/III-V heterogeneous integration. *APL Photonics* **4**, 111101 (2019).
- Porter C, Zeng S, Zhao X et al. Hybrid integrated chip-scale laser systems. *APL Photonics* **8**, 080902 (2023).
- Billah MR, Blaicher M, Hoose T et al. Hybrid integration of silicon photonics circuits and InP lasers by photonic wire bonding. *Optica* **5**, 876–883 (2018).
- Tanaka S, Jeong SH, Sekiguchi S et al. High-output-power, single-wavelength silicon hybrid laser using precise flip-chip bonding technology. *Opt Express* **20**, 28057–28069 (2012).
- Corato-Zanarella M, Gil-Molina A, Ji XC et al. Widely tunable and narrow-linewidth chip-scale lasers from near-ultraviolet to near-infrared wavelengths. *Nat Photonics* **17**, 157–164 (2023).
- Guan H, Novack A, Galfsky T et al. Widely-tunable, narrow-linewidth III-V/silicon hybrid external-cavity laser for coherent communication. *Opt Express* **26**, 7920–7933 (2018).
- Hulme JC, Doylend JK, Bowers JE. Widely tunable Vernier ring laser on hybrid silicon. *Opt Express* **21**, 19718–19722 (2013).
- Zhao RL, Guo YY, Lu LJ et al. Hybrid dual-gain tunable integrated InP-Si<sub>3</sub>N<sub>4</sub> external cavity laser. *Opt Express* **29**, 10958–10966 (2021).
- Guo YY, Zhao RL, Zhou GQ et al. Thermally tuned high-performance III-V/Si<sub>3</sub>N<sub>4</sub> external cavity laser. *IEEE Photonics J* **13**, 1500813 (2021).
- Fan YW, van Rees A, van der Slot PJM et al. Hybrid integrated InP-Si<sub>3</sub>N<sub>4</sub> diode laser with a 40-Hz intrinsic linewidth. *Opt Express* **28**, 21713–21728 (2020).
- Li MX, Chang L, Wu L et al. Integrated Pockels laser. *Nat Commun*

- 13, 5344 (2022).
21. Han Y, Zhang X, Huang FJ et al. Electrically pumped widely tunable O-band hybrid lithium niobate/III-V laser. *Opt Lett* **46**, 5413–5416 (2021).
  22. Wan YT, Zhang S, Norman JC et al. Tunable quantum dot lasers grown directly on silicon. *Optica* **6**, 1394–1400 (2019).
  23. Guo YY, Li XH, Jin MH et al. Hybrid integrated external cavity laser with a 172-nm tuning range. *APL Photonics* **7**, 066101 (2022).
  24. Zhang M, Wang C, Cheng R et al. Monolithic ultra-high-Q lithium niobate microring resonator. *Optica* **4**, 1536–1537 (2017).
  25. Wu RB, Zhang JH, Yao N et al. Lithium niobate micro-disk resonators of quality factors above  $10^7$ . *Opt Lett* **43**, 4116–4119 (2018).
  26. Desiatov B, Shams-Ansari A, Zhang M et al. Ultra-low-loss integrated visible photonics using thin-film lithium niobate. *Optica* **6**, 380–384 (2019).
  27. Wang C, Zhang M, Chen X et al. Integrated lithium niobate electro-optic modulators operating at CMOS-compatible voltages. *Nature* **562**, 101–104 (2018).
  28. Zhang M, Buscaino B, Wang C et al. Broadband electro-optic frequency comb generation in a lithium niobate microring resonator. *Nature* **568**, 373–377 (2019).
  29. Han JL, Li MQ, Wu RB et al. High fiber-to-fiber net gain in erbium-doped thin film lithium niobate waveguide amplifier as an external gain chip. *Opto-Electron Sci* **4**, 250004 (2025).
  30. Huang HJ, Balčytis A, Dubey A et al. Spatio-temporal isolator in lithium niobate on insulator. *Opto-Electron Sci* **2**, 220022 (2023). doi: [10.29026/oes.2023.220022](https://doi.org/10.29026/oes.2023.220022).
  31. Fu BT, Gao RH, Yao N et al. Soliton microcomb generation by cavity polygon modes. *Opto-Electron Adv* **7**, 240061 (2024).
  32. Chakkoria JJ, Dubey A, Mitchell A et al. Ferroelectric domain engineering of Lithium niobate. *Opto-Electron Adv* **8**, 240139 (2025).
  33. Yang QX, Yu MH, Chen ZX et al. A novel approach towards robust construction of physical colors on lithium niobate crystal. *Opto-Electron Adv* **8**, 240193 (2025).
  34. He MB, Xu MY, Yao YX et al. High-performance hybrid silicon and lithium niobate Mach-Zehnder modulators for 100 Gbit·s<sup>-1</sup> and beyond. *Nat Photonics* **13**, 359–364 (2019).
  35. Yu MJ, Barton III D, Cheng R et al. Integrated femtosecond pulse generator on thin-film lithium niobate. *Nature* **612**, 252–258 (2022).
  36. Zhu D, Shao LB, Yu MJ et al. Integrated photonics on thin-film lithium niobate. *Adv Opt Photonics* **13**, 242–352 (2021).
  37. Lin JT, Bo F, Cheng Y et al. Advances in on-chip photonic devices based on lithium niobate on insulator. *Photonics Res* **8**, 1910–1936 (2020).
  38. Xie ZD, Bo F, Lin JT et al. Recent development in integrated Lithium niobate photonics. *Adv Phys X* **9**, 2322739 (2024).
  39. Boes A, Chang L, Langrock C et al. Lithium niobate photonics: unlocking the electromagnetic spectrum. *Science* **379**, eabj4396 (2023).
  40. Kösters M, Sturman B, Werheit P et al. Optical cleaning of congruent lithium niobate crystals. *Nat Photonics* **3**, 510–513 (2009).
  41. Yu SP, Fang ZW, Wang Z et al. On-chip single-mode thin-film lithium niobate Fabry-Perot resonator laser based on Sagnac loop reflectors. *Opt Lett* **48**, 2660–2663 (2023).
  42. Zhu YR, Yu SP, Fang ZW et al. Integrated electro-optically tunable narrow-linewidth III-V laser. *Adv Photonics Res* **5**, 2400018 (2024).
  43. Huang QF, Fang ZW, Wang Z et al. On-chip tunable single-mode high-power narrow-linewidth Fabry-Perot microcavity laser on Yb<sup>3+</sup>-doped thin-film lithium niobate. *Photonics Res* **13**, 935–940 (2025).
  44. Song LB, Chen JM, Wu RB et al. Electro-optically tunable optical delay line with a continuous tuning range of ~220 fs in thin-film lithium niobate. *Opt Lett* **48**, 2261–2264 (2023).
  45. Wang M, Wu RB, Lin JT et al. Chemo-mechanical polish lithography: a pathway to low loss large-scale photonic integration on lithium niobate on insulator. *Quantum Eng* **1**, e9 (2019).
  46. Wu RB, Wang M, Xu J et al. Long low-loss-litium niobate on insulator waveguides with sub-nanometer surface roughness. *Nanomaterials* **8**, 910 (2018).
  47. Mortimore DB. Fiber-optic wavelength. *J Lightwave Technol* **6**, 1217–1224 (1988).
  48. Zheng Y, Zhong HZ, Zhang HS et al. Electro-optically programmable photonic circuits enabled by wafer-scale integration on thin-film lithium niobate. *Phys Rev Res* **5**, 033206 (2023).
  49. Du BX. *Theoretical Foundations of Semiconductor Lasers* (Science Press, Beijing, 2011).

## Acknowledgements

We are grateful for financial supports from National Key Research and Development Program of China (2022YFA1205100); National Natural Science Foundation of China (12192251, 12334014, 92480001, 12274133); Quantum Science and Technology-National Science and Technology Major Project (2021ZD0301403); Shanghai Municipal Science and Technology Major Project (2019SHZDZX01); Fundamental Research Funds for The Central Universities; The Engineering Research Center for Nanophotonics & Advanced Instrument, Ministry of Education, East China Normal University (No. 2023nmc005).

## Author contributions

Y.Z., Y.C. and Z.F. conceived the idea and concept. Y.Z. and Q.H. performed the experiments. Y.Z. and B.F. designed the TFLN chip. Y.Z. and B.F. carried out the data analysis and simulations. Y.Z., Y.L., J.Y., Y.M. and Y.S. fabricated the TFLN chip. Y.Z. wrote the manuscript with assistance from Y.C., Z.F., M.W., Z.X. and K.J. and input from all co-authors. Y.C. supervised the project.

## Competing interests

The authors declare no competing financial interests.

## Supplementary information

Supplementary information for this paper is available at <https://doi.org/10.29026/oea.2026.250274>



**Open Access** This article is licensed under a Creative Commons Attribution 4.0 International License, which permits use, sharing, adaptation, distribution and reproduction in any medium or format, as long as you give appropriate credit to the original author(s) and the source, provide a link to the Creative Commons license, and indicate if changes were made. To view a copy of this license, visit <http://creativecommons.org/licenses/by/4.0/>

©The Author(s) 2026.

Published by Editorial Office of *Opto-Electronic Advance*, Institute of Optics and Electronics, Chinese Academy of Sciences.

